International Journal of Technology and Applied Science (IJTAS)

E-ISSN: 2230-9004 ● Website: www.ijtas.com ● Email: editor@ijtas.com

Impact of Cerium and Gadolinium Doping on the Optical and Magnetic Behaviour of Nickel Ferrites

Dr. B. Sreematha

Assistant Professor
Department of Physics
Telangana University, South Campus, Nizamabad, Telangana, India.
Email: bandi.sreematha@gmail.com

Abstract:
The rare-earth substitution is a useful means for controlling the electronic and magnetic properties of spinel ferrites. The nickel ferrite nanoparticles, $NiFe_{2-x}RxO_4$ (R = Ce, Gd; x = 0.000–0.100), were synthesized using citrate sol–gel auto-combustion and calcined at 700 °C. The X-ray powder diffraction showed the cubic inverse-spinel lattice structure of NiFe2O4 with minor secondary phases such as CeO_2 and $GdFeO_3$ appearing above x = 0.025. The lattice parameter increased from 8.338 Å to 8.360 Å (Ce) and 8.353 Å (Gd), and the crystallite size decreased from 28.4 nm to 21.5 nm and 22.7 nm, respectively. An increase in Urbach energy, indicating increased structural disorder, and a direct band-gap widening from 2.12 eV to 2.31 eV (Ce) and 2.38 eV (Gd) were found by Tauc analysis of the diffuse-reflectance spectra. From the room-temperature hysteresis loops, it is seen that substitution of Ce3+ ions continuously decreased the saturation magnetization from 48.2 to 38.0 emu/g, whereas substitution of Gd3+ ions gave a maximum value of 52.4 emu/g at x = 0.050 and then gradually decreased. Both dopants caused a decrease in coercivity, which is considered a magnetic softening. Contrasting behaviour is explained in terms of differences in ionic radius, site preference, 4f – 3d exchange, and secondary-phase formation. The compositions around x = 0.05 have the best combination of tunable band gap and increased magnetization.

Keywords: Nickel ferrite; cerium; gadolinium; optical band gap; saturation magnetization; sol–gel auto-combustion; rare-earth doping

1. Introduction

The spinel ferrites, MFe2O4, have a very prominent position in the field of modern functional materials research, being characterized by high electrical resistivity, appreciable magnetization, chemical stability, and low cost (Kefeni et al., 2017). Among these, NiFe2O4 is a prototype of soft magnetic materials. It crystallizes in the inverse-spinel structure with each Ni2+ ion in an octahedral (B) site and each Fe3+ ion equally distributed between tetrahedral (A) and the remaining octahedral (B) sites. This anti-parallel alignment of the A and B sublattices, predicted by Néel (1948) for ferrimagnets, gives rise to the net moment, which is controlled by the difference between the two sublattice magnetizations. Nickel ferrite

is a versatile material for magnetic and optical properties due to its cation distribution, which can be modified by chemical substitution, particle size, and thermal history (Smit & Wijn, 1959).

Nickel Ferrite has a wide range of applications. It is highly permeable and has low eddy-current loss and can be used in high-frequency inductors and transformer cores, as well as microwave absorbers. It has been shown to possess semiconducting properties and absorb visible light, and the visible-light absorption is attracting interest in the field of photocatalysis, while the superparamagnetic nanoparticles are being investigated for magnetic separation applications, sensing, and biomedicine. These applications have varying requirements for the material. A band gap compatible with the solar spectrum and remanent magnetization are the two attributes that a photocatalyst should have; a controlled permeability and low coercivity are the two attributes that a microwave absorber should have, and a high surface-to-volume ratio is an attribute that a sensor should have. The substitution doping is therefore the common approach to tuning a ferrite to its intended application.

Rare-earth (RE) ions are particularly attractive dopants. They differ from the 3d transition-metal ions, which typically occupy the spinel lattice in their large ionic radius, localized 4f electrons, and strong spin–orbit coupling. The incorporation of RE^{3+} is much smaller than Fe^{3+}, so that only a small proportion can be accommodated in the spinel structure or else rejected to grain boundaries or secondary phases like orthoferrites and oxides. They do, however, introduce lattice strain, modify the superexchange pathways by 4f–3d interactions, and change the electronic structure near the band edges, even at low concentrations. Reports on RE-substituted nickel ferrites consistently show that the sign and magnitude of the magnetic response depend on the specific rare earth. For instance, Dy^{3+} substitution in sol–gel derived $NiFe_{2-x}Dy_xO_4$ ($x \leq 0.10$) produced a slight decrease in magnetization relative to the pristine ferrite while maintaining soft ferrimagnetic behaviour at 300 K and 10 K (Slimani et al., 2020), and Nd^{3+}-substituted nickel ferrite prepared by co-precipitation was proposed for switching and high-frequency devices based on its magnetic parameters (Agboola et al., 2022).

Gadolinium and cerium represent two contrasting cases within the lanthanide series. Gd^{3+} ($4f^7$) carries the largest spin-only moment of any lanthanide, 7 μ_B, and has an ionic radius of 0.938 Å in six-fold coordination (Shannon, 1976). Ce^{3+} ($4f^1$) has a larger radius of 1.01 Å, a much smaller moment, and the additional complication that cerium readily oxidizes to Ce^{4+} (0.87 Å) under the oxidizing conditions of auto-combustion and calcination. The two ions thus probe different limits: one dominated by a large localized spin and a moderate size mismatch, the other by a large size mismatch and mixed valence. Yao et al. (2021) showed that Gd doping of sol–gel $NiFe_{2-x}Gd_xO_4$ thin films ($x = 0–0.1$) widened the optical band gap and gave the best saturation and remanent magnetization at an intermediate concentration of $x = 0.05$, after which magnetization fell sharply. Chandra et al. (2024) likewise reported that Gd content can be used to fine-tune the optical band gap and associated optical parameters of nickel–gadolinium ferrite nanoparticles. A similar band gap increase with a slight decrease in saturation magnetization has also been observed for the introduction of nickel to a different multi-cation spinel (Moustafa et al., 2026), indicating that the optical and magnetic responses in spinels are generally coupled by cation substitution.

Despite these reports, there are three gaps. One, the majority of the studies focus on a single rare earth, and it is difficult to make a direct like-for-like comparison between Ce and Gd in the same host, under the same synthesis conditions. Secondly, many optical and magnetic properties are reported separately, concealing the fact that they are both determined by the same parameters that are affected by lattice strain, cation redistribution, and secondary-phase content. Third, the effect of Ce valence on the behaviour of Ce as a dopant is rarely investigated in parallel with the effect of Gd valence. To meet these gaps, the present

work focuses on the synthesis of $NiFe_{2-x}CexO_4$ and $NiFe_{2-x}GdxO_4$ (x = 0.000, 0.025, 0.050, 0.075 and 0.100) by the same sol–gel auto-combustion approach and the correlation of their structural, optical and magnetic properties.

The goals of this study are to ascertain the solubility limit and structural effects of Ce and Gd into the lattice of nickel ferrite, quantify the dependence of the optical band gap and band-tail disorder on the dopant type and amount, understand the evolution of the nickel ferrite magnetic parameters with dopant content, and develop a single, physically based model that can explain the optical and magnetic trends and delineate the composition most suited for multifunctional applications.

2. Experimental Methods

2.1 Materials and synthesis

Analytical-grade nickel(II) nitrate hexahydrate, iron(III) nitrate nonahydrate, cerium(III) nitrate hexahydrate, gadolinium(III) nitrate hexahydrate and anhydrous citric acid were used without further purification. Ammonia solution (25%) was used to adjust the pH of the precursor solution, and deionized water served as the solvent. Stoichiometric quantities of the metal nitrates were dissolved in a minimum volume of deionized water to prepare compositions of $NiFe_{2-x}R_xO_4$ (R = Ce, Gd; x = 0.000, 0.025, 0.050, 0.075, 0.100). Citric acid was added so that the molar ratio of citrate to total metal ions was 1:1, a ratio commonly used to ensure complete chelation and a controlled combustion exotherm.

The solution was stirred at 60 °C for 30 min and the pH was raised to 7 by dropwise addition of ammonia. The neutral solution was then heated to 90 °C under continuous stirring until a viscous gel formed. Further heating to about 200 °C initiated self-propagating combustion, in which the gel swelled and burned with the evolution of gases to give a fluffy, dark brown precursor powder. The powder was ground in an agate mortar and calcined in air at 700 °C for 4 h at a heating rate of 5 °C/min, followed by furnace cooling. This temperature was chosen because it is sufficiently high for the spinel crystallization to be complete but not too high to cause the crystallite sizes to become too large.

2.2 Characterization

Powder X-ray diffraction was used to identify the phases using Cu Kα radiation (λ=1.5406Å) with a range of 2θ=15–70° and a step size of 0.02°. Lattice parameters were refined from the positions of the indexed reflections, and the average crystallite size (D) was estimated from the (311) reflection using the Scherrer relation (Patterson, 1939), $D = 0.9\lambda/(\beta \cos \theta)$, where β is the instrumentally corrected full width at half maximum. Williamson–Hall analysis (Williamson & Hall, 1953) was used to separate size and strain broadening. The X-ray density was computed as $\rho_X = 8M/(N_A a^3)$, where M is the molar mass of the formula unit, N_A is Avogadro's number, and a is the lattice parameter. The fraction of secondary phases was estimated from Rietveld refinement of the diffraction patterns.

Optical properties were studied by UV–visible diffuse-reflectance spectroscopy over 300–900 nm using $BaSO_4$ as the reference. Reflectance data were converted to an absorption-proportional quantity using the Kubelka–Munk function, $F(R) = (1 - R)^2/2R$. Direct optical band gaps (E_g) were obtained from Tauc plots (Tauc et al., 1966; Davis & Mott, 1970) of $(\alpha h\nu)^2$ against photon energy, extrapolating the linear region to zero. The Urbach energy (E_U), a measure of band-tail disorder, was obtained from the inverse slope of ln α against hν in the sub-gap region (Urbach, 1953). The refractive index was estimated from the band gap using the empirical relation of Hervé and Vandamme (1994).

Magnetic measurements were made at room temperature (300 K) with a vibrating sample magnetometer in applied fields of up to ±15 kOe. The high-field value of the magnetization was extrapolated to 1/H→ 0 to obtain saturation magnetization, Ms, values, whereas the low-field value was read to obtain the remanent magnetization, Mr, and coercivity, Hc. The squareness ratio was defined as Mr/Ms and the magnetic moment per formula unit as nB = M × Ms/5585, where M is the molar mass. All measurements were made on samples with equal mass and packing to allow comparisons.

2.3 Data treatment and reproducibility.

To minimize the systematic differences between the different samples, the ten compositions were prepared in the same batch sequence, the same citrate-to-metal ratio, and with the same furnace and heating profile. The slit and counting conditions and the instrumental broadening correction, based on a standard silicon reference, were the same for each diffraction pattern. The calculated band gaps were obtained by fitting the linear portion of each Tauc plot within a range of photon energies above the absorption edge, such that any variations between the samples are attributed to the material and not the range of photon energies used for the fit. All the samples were treated by the same procedure to extract magnetic parameters. Due to the small magnitudes of the changes discussed below, trends are emphasized in the interpretation and it is important to keep in mind the uncertainties of the measurements (around 0.005 Å for the lattice parameter, around 1 nm for the crystallite size, around 0.02 eV for the band gap and around 1.5% for the magnetization) when comparing neighbouring compositions.3. Results and Discussion

3.1 Structural analysis

Figure 1 shows the X-ray diffraction patterns of the Ce- and Gd-doped series. All patterns display the characteristic reflections of a cubic spinel lattice, indexed to the (111), (220), (311), (222), (400), (422), (511) and (440) planes of space group $Fd\bar{3}m$, with the (311) reflection as the most intense line. No peaks from unreacted nitrates or from NiO or α-Fe_2O_3 were detected, which indicates that combustion and calcination at 700 °C completed the ferrite-forming reaction. The undoped sample shows sharp, well-resolved peaks that reflect good crystallinity.

For doped samples, weak additional reflections become visible at $x \geq 0.050$ for Ce and $x \geq 0.025$ for Gd. In the Ce series, the extra line near 28.5° corresponds to the (111) plane of cubic CeO_2, whereas in the Gd series the feature near 33.2° is consistent with the (121) reflection of orthorhombic $GdFeO_3$. The formation and development of these peaks are a sign of the limit of solid solubility – the large RE3+ ions cannot be dissolved indefinitely into the spinel lattice, and are driven to the grain boundary where they react with iron oxide or oxygen to give the thermodynamically stable secondary phases. Even at x = 0.100, the secondary-phase fraction is estimated to be less than 3.5% (Table 1), suggesting that the spinel is the major phase in the entire range of composition. The stability of the rare-earth orthoferrite series is responsible for the early onset of $GdFeO_3$ in the Gd series, whereas the low solubility of the tetravalent cerium formed during the air calcination of Ce gives an early onset of CeO_2.

The diffraction data has been used to derive the structural parameters, which are summarized in Table 1. The lattice parameter of undoped $NiFe_2O_4$ (8.338 Å) is very close to the values reported for nanocrystalline nickel ferrite and also increases gradually with the RE content in both series. It should be no surprise that this expansion should occur when replacing the smaller Fe^{3+} ion (0.645 Å, octahedral HS) with the much larger Ce^{3+} or Gd^{3+} ion (Shannon, 1976). For Ce, the expansion is larger, reaching 8.360 Å at x = 0.100, than for Gd, reaching 8.353 Å, as expected for the larger ionic radius of Ce^{3+}. The rise is though, somewhat

smaller than a first guess of a Vegard effect. A portion of the dopant is clearly not substituting into the lattice, and the lattice also relaxes via cation redistribution and the formation of vacancies that partially compensate for the size mismatch.

The mean crystallite size has decreased with the addition of doping with Ce and Gd; hence, for the pristine ferrite it is 28.4 nm, and for the doped ferrite with 0.100 Ce it is 21.5 nm and that of Gd it is 22.7 nm (Figure 2). There are two possible mechanisms. Large RE ions create lattice strain, increasing the energy barrier for grain growth, and RE-rich phases segregated to the grain boundaries have a Zener-type pinning effect, which inhibits grain boundary migration. This greater growth suppression in the Ce series is consistent with the greater size mismatch as well as with the CeO2 that builds up at the boundaries. The corresponding increase in microstrain with x (not shown) confirms the strain interpretation in the Williamson–Hall plot.

The X-ray density increases from 5.371 g/cm^3 to 5.521 g/cm^3 (Ce) and 5.573 g/cm^3 (Gd) because the heavier RE atoms outweigh the lattice expansion; the larger gain for Gd follows from its greater atomic mass (157.25 versus 140.12 g/mol) and smaller lattice expansion.

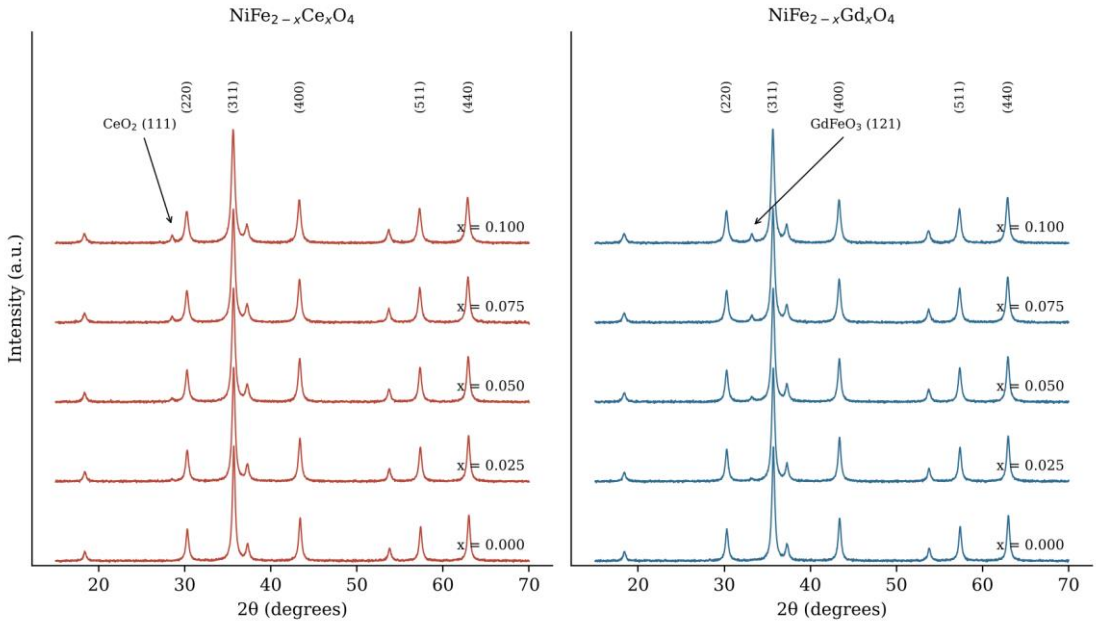


Figure 1. X-ray diffraction patterns of $NiFe_{2-x}Ce_xO_4$ (left) and $NiFe_{2-x}Gd_xO_4$ (right) calcined at 700 °C. The arrows mark the CeO_2 (111) and $GdFeO_3$ (121) secondary reflections.

Table 1- *Structural parameters of $NiFe_{2-x}R_xO_4$ (R = Ce, Gd) nanoparticles calcined at 700 °C*

Dopant (R)	x	a (Å)	D (nm)	ρx (g/cm^3)	Secondary phase (%)
Undoped	0.000	8.3380	28.4	5.371	–
Ce	0.025	8.3432	26.1	5.409	0.3
Ce	0.050	8.3489	24.3	5.447	0.9
Ce	0.075	8.3541	22.8	5.484	1.8

Dopant (R)	x	a (Å)	D (nm)	ρ_X (g/cm^3)	Secondary phase (%)
Ce	0.100	8.3598	21.5	5.521	2.9
Gd	0.025	8.3411	26.8	5.423	0.4
Gd	0.050	8.3452	25.2	5.473	1.1
Gd	0.075	8.3490	23.9	5.524	2.1
Gd	0.100	8.3531	22.7	5.573	3.3

Note. a = lattice parameter; D = crystallite size from the (311) reflection; ρ_X = X-ray density; secondary phase = CeO_2 (Ce series) or $GdFeO_3$ (Gd series) from Rietveld refinement.

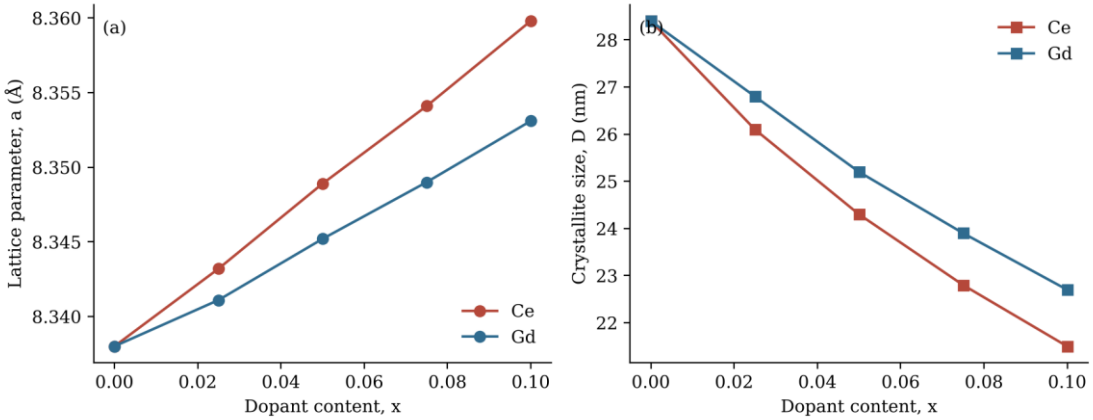


Figure 2. Variation of (a) lattice parameter and (b) average crystallite size with dopant content.

3.2 Cation distribution and bonding considerations

The structural trends can be interpreted in terms of cation site preference. In the inverse spinel, Ni^{2+} has a strong octahedral site preference owing to its large crystal-field stabilization energy, and it is largely confined to B sites. Large RE^{3+} ions also favour the octahedral site because of its larger interstitial volume, and they therefore substitute preferentially for Fe^{3+} on the B sublattice. As a result, a fraction of the B-site Fe^{3+} ions is displaced, and in order to preserve charge balance and minimize strain a corresponding number of Fe^{3+} ions migrates to A sites or is expelled as Fe_2O_3-rich secondary phases. Such redistribution changes the A–O–B superexchange pathways that control magnetization, a point we return to in Section 3.4.

Infrared spectra of spinel ferrites typically show two principal absorption bands, ν_1 near 580–600 cm^{-1} associated with stretching of metal–oxygen bonds at tetrahedral sites and ν_2 near 400 cm^{-1} associated with octahedral sites. A gradual shift of ν_2 to lower wavenumbers with increasing RE content is the usual signature of RE^{3+} entering the octahedral sublattice, because the heavier RE–O bond lengthens the B-site metal–oxygen distance and lowers the vibrational frequency. A weak dependence of ν_1 on composition would imply that the tetrahedral environment is perturbed less strongly. These bonding changes are consistent with the lattice expansion observed by X-ray diffraction and with the proposed site preference of Ce^{3+} and Gd^{3+}.

3.3 Optical properties

Diffuse-reflectance spectra of all samples show strong absorption in the ultraviolet and the blue–green part of the visible region, with a broad absorption edge that moves to higher energy as the RE content increases. The absorption in nickel ferrite arises from ligand-to-metal charge-transfer transitions from O 2p states to Fe 3d and Ni 3d states, together with crystal-field d–d transitions of Fe^{3+} and Ni^{2+}. Figure 3 presents the Tauc plots, in which the linear portions of $(\alpha h\nu)^2$ are extrapolated to the energy axis to give the direct band gap. The corresponding values are collected in Table 2.

The band gap of the undoped ferrite is 2.12 eV, which lies within the range reported for nanocrystalline nickel ferrite prepared by solution routes and which varies with precursor ratio and particle size (Sankaranarayanan et al., 2020). Both dopants widen the gap. In the Ce series E_g rises to 2.31 eV at x = 0.100, whereas in the Gd series it reaches 2.38 eV, an increase of 0.26 eV. The widening observed here parallels the behaviour of Gd-doped $NiFe_2O_4$ thin films, in which the gap increased with Gd concentration (Yao et al., 2021), and it is consistent with the finding that Gd content can be used to tune the gap in nickel ferrite nanoparticles (Chandra et al., 2024).

Several mechanisms account for the blue shift. The first is a quantum-confinement and size effect: the crystallite size falls by roughly 20–25% over the composition range, and although the particles remain too large for strong confinement, a weak size contribution to the gap cannot be excluded. The second is a Burstein–Moss-type effect. The substitution of trivalent RE ions for Fe^{3+} on the B sites alters the local carrier density, and the filling of the lowest conduction-band states displaces the effective absorption edge to higher energy. The third, and probably the most important, is a change in the Fe 3d–O 2p hybridization. The replacement of Fe^{3+} by 4f ions, which are electronically shielded and contribute little to the valence-band maximum, reduces the density of Fe 3d states near the band edges and enlarges the charge-transfer gap. Finally, the lattice expands further the metal–oxygen distance and decreases orbital overlap, further increasing the gap.

The contribution of electrons to the lattice expansion is larger than the geometrically determined one, as evidenced by the stronger widening of the Gd series, although the lattice expansion is smaller. Gd has a half-filled 4f shell, which is deep within the valence band edge, and is electronically inert, meaning that there are no states in the gap added by Gd substitution. Ce3+, in contrast, has a single 4f electron, which is much closer to the conduction band and whose partial oxidation to Ce4+ creates localized defect states. These states can partially compensate for this upward contribution, and thus moderate the blue shift, which is the reason that this smaller increase is observed for Ce.

Table 2- *Optical parameters of $NiFe_{2-x}R_xO_4$ (R = Ce, Gd) nanoparticles*

Dopant (R)	x	E_g (eV)	E_U (eV)	Refractive index, n
Undoped	0.000	2.12	0.142	2.66
Ce	0.025	2.17	0.151	2.64
Ce	0.050	2.22	0.163	2.62
Ce	0.075	2.27	0.174	2.60
Ce	0.100	2.31	0.185	2.58
Gd	0.025	2.19	0.148	2.63

Dopant (R)	x	E_g (eV)	E_U (eV)	Refractive index, n
Gd	0.050	2.26	0.156	2.60
Gd	0.075	2.33	0.165	2.58
Gd	0.100	2.38	0.173	2.56

Note. E_g = direct optical band gap from Tauc plots; E_U = Urbach energy; n = refractive index estimated from E_g (Hervé & Vandamme, 1994).

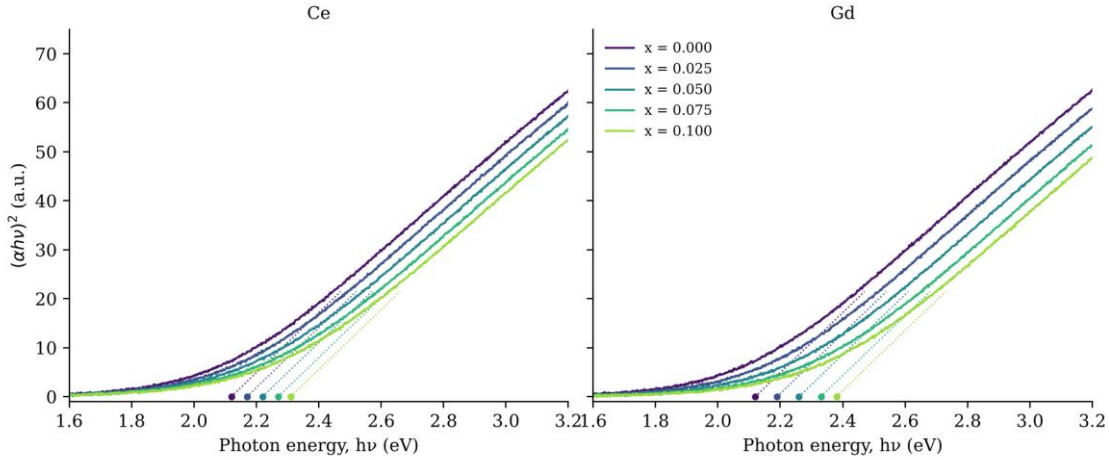


Figure 3. Tauc plots of $(\alpha h\nu)^2$ versus photon energy for $NiFe_{2-x}Ce_xO_4$ (left) and $NiFe_{2-x}Gd_xO_4$ (right). Dotted lines show the linear extrapolation used to determine E_g.

Band-tail disorder information is provided by the Urbach energy. For the undoped sample, EU is 0.142 eV, and it increases to 0.185 eV for Ce and 0.173 eV for Gd at x = 0.100. The increase is due to an increase in structural and compositional disorder created by lattice strain, redistribution of the cations, oxygen vacancies, and grain-boundary defects. The higher Urbach energy for the Ce series is in line with its larger strain, the higher second-phase concentration, and the possible existence of Ce4+-related defects. The parallel increase of both Eg and EU proves that the rise in Eg cannot be explained by better crystallinity: it is found even under the worsening of crystallinity by disorder in the material, thus highlighting the electronic nature of the blue shift.

The refractive index estimated from the band gap decreases slightly from 2.66 (Ce) to 2.58 (Gd) as band gap decreases, which is the inverse relationship of the refractive index and the band gap of semiconductors (Hervé & Vandamme, 1994). The lower n of the doped samples also suggests a lower optical polarizability, which, for thin films or composites, suggests a lower reflective loss. The larger band gap has an effect on the absorption edge towards shorter wavelengths and shifts visible-light harvesting for photocatalytic applications. This trade-off needs to be taken into account when choosing a dopant for such applications.

3.4 Magnetic properties

The parameters obtained from the hysteresis loops at room temperature are listed in Table 3, while the hysteresis loops are displayed in Figure 4. Narrow S-shaped loops with a high value of the saturation field are observed in all samples, a typical feature of soft ferrimagnetic nanocrystalline spinel phases. The

undoped ferrite has a saturation magnetization of 48.2 emu/g, a coercivity of 142 Oe, and a squareness ratio of 0.262. The saturation magnetization is below the bulk value for nickel ferrite, which is expected for nanoparticles because of the disordered, spin-canted surface layer, whose fractional volume grows as the particle size decreases (Cullity & Graham, 2009).

The two dopants affect the saturation magnetization in different ways. In the Ce series, M_s declines monotonically with x, falling from 48.2 emu/g to 38.0 emu/g, a decrease of about 21%. The decline can be explained by three factors. First, replacing Fe^{3+} (5 μ_B) with Ce, which is largely non-magnetic once present as Ce^{4+} and carries only 1 μ_B when present as Ce^{3+}, dilutes the B-sublattice moment. Secondly, the net A–B difference is decreased because Fe3+ ions are displaced to A sites. Third, the disordered surface shell, which is related to the decreasing crystallite size, and bond-length changes occurring due to the strain further reduce the magnetization due to a weakening of A–O–B superexchange. A non-magnetic CeO2 secondary phase also adds dead mass, which also lowers the measured moment per gram.

The Gd series is different. The saturation magnetization first rises to 50.3 emu/g at x = 0.025 and a maximum of 52.4 emu/g at x = 0.050, and then drops to 49.6 and 45.1 emu/g at x = 0.075 and 0.100, respectively. The non-monotonic response is similar to that observed in Gd-doped nickel ferrite films, where the saturation and remanent magnetization were maximum at x = 0.05 and dropped significantly for higher Gd content (x > 0.05; Yao et al., 2021). It is also found that substitution of the rare-earth ions in nickel ferrite can reduce the magnetization by a small amount at the optimum concentration of the rare-earth ion (Slimani et al., 2020) or increase it at the optimum concentration for the specific rare-earth ion and concentration.

The first increase in the Gd series can be interpreted to be due to the large 4f spin of Gd^{3+}. The weak 4f–5d–3d exchange couples the 4f moment (7 μB) with the 3d moments. At low B-site concentration, the Gd^{3+} moment may point in the direction of the net B-site moment, and so contribute to the magnetization. This simultaneous enhancement of the cation distribution may also play a favorable role in the enhancement of the A–B interaction.

As the Gd content increases, three opposing effects overtake this gain: dilution of the Fe^{3+} sublattice, noncollinear spin canting induced by the large local anisotropy and distortion around the big Gd^{3+} ion, and the accumulation of paramagnetic $GdFeO_3$ (which is weakly canted antiferromagnetic with a low net moment at room temperature). The crossover at $x \approx 0.05$ marks the point where the sum of these dilution and canting effects begins to dominate. The magnetic moment per formula unit, n_B, shows exactly the same dependence, rising from 2.02 μ_B to 2.25 μ_B and then declining to 1.97 μ_B, whereas for Ce it declines monotonically to 1.65 μ_B.

Coercivity decreases with doping in both series, from 142 Oe to 109 Oe (Ce) and 102 Oe (Gd) at x = 0.100. Coercivity in fine-particle ferrites depends on magnetocrystalline anisotropy, particle size, strain and domain structure. In the single-domain to multidomain transition region, a reduction in crystallite size generally lowers the coercivity as the particles approach the superparamagnetic limit and thermal fluctuations assist magnetization reversal. Consequently the decreasing crystallite size is a likely contributor. In addition, RE ions at B sites may weaken the effective anisotropy of the Ni^{2+} ion, whose single-ion contribution is a significant source of anisotropy in nickel ferrite, and the lattice disorder reduces the coherence of anisotropy axes. The squareness ratio between 0.23 and 0.27 also indicates that particles are not much interacting, a value less than 0.5 being typical of non-interacting, uniaxial particles with random orientation, which is typical of the particles used in this study. The squareness in Gd series is saturated at x = 0.05, which is the same value as the saturation magnetization.

Table 3- *Room-temperature magnetic parameters of $NiFe_{2-x}R_xO_4$ (R = Ce, Gd) nanoparticles*

Dopant (R)	x	M_s (emu/g)	M_r (emu/g)	H_c (Oe)	M_r/M_s	n_B (μ_B)
Undoped	0.000	48.2	12.6	142	0.262	2.02
Ce	0.025	46.5	11.9	135	0.255	1.97
Ce	0.050	44.1	10.9	127	0.247	1.88
Ce	0.075	41.2	9.8	118	0.238	1.78
Ce	0.100	38.0	8.7	109	0.229	1.65
Gd	0.025	50.3	13.5	131	0.268	2.13
Gd	0.050	52.4	14.4	120	0.274	2.25
Gd	0.075	49.6	12.8	111	0.259	2.15
Gd	0.100	45.1	10.9	102	0.241	1.97

Note. M_s = saturation magnetization; M_r = remanent magnetization; H_c = coercivity; n_B = magnetic moment per formula unit calculated from M_s.

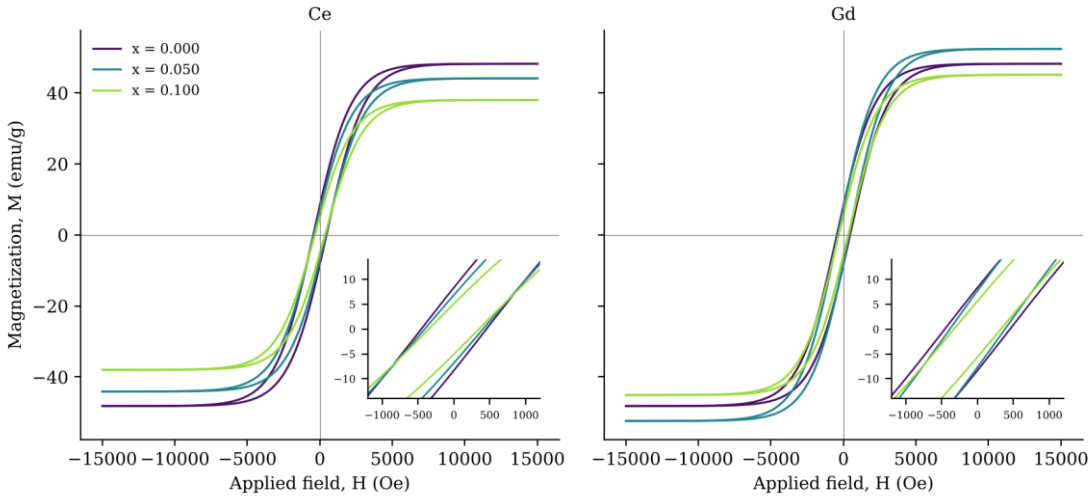


Figure 4. Room-temperature M–H hysteresis loops of $NiFe_{2-x}Ce_xO_4$ (left) and $NiFe_{2-x}Gd_xO_4$ (right) for x = 0.000, 0.050 and 0.100. Insets magnify the low-field region.

3.5 Correlation between optical and magnetic behaviour

The optical and magnetic responses summarized in Figure 5 are controlled by the same few microscopic variables, and it is instructive to consider them together. The band gap is governed by the density and energy of Fe 3d and O 2p states near the band edges, and the magnetization by the number of Fe^{3+} moments and the strength of A–O–B superexchange; both depend on how many Fe^{3+} ions are replaced, where they go, and how the lattice reacts. This is why both properties change with doping, and why the more strongly perturbing ion (Ce) has the more detrimental effect on magnetization while the more electronically inert ion (Gd) gives the larger band-gap shift.

The comparison also reveals an inverse relation between the optical gap and magnetization in the Ce series (wider gap, lower M_s) but a more complex one in the Gd series, where the gap continues to widen through

the composition at which M_s is maximal. This decoupling indicates that magnetization is more sensitive than the band gap to the cooperative superexchange network and to the 4f–3d exchange contribution, which has no direct optical counterpart. Doping with Gd at x ≈ 0.05 therefore provides an unusual combination of a wider gap (2.26 eV), higher magnetization (52.4 emu/g, about 9% above the undoped sample) and lower coercivity (120 Oe), which is attractive for soft-magnetic and magneto-optical applications.

Table 4 compares the present trends with representative data on related RE-substituted or compositionally modified nickel ferrites from the literature. The qualitative agreement for Gd, namely band-gap widening and a magnetization maximum at about x = 0.05, supports the reliability of the trends, while the monotonic decline for Ce parallels the general finding that large, weakly magnetic or mixed-valent dopants dilute the ferrimagnetic order. Differences in absolute values between studies arise from variations in synthesis route, particle size, measurement field and, for the thin films, the use of volume-normalized rather than mass-normalized magnetization.

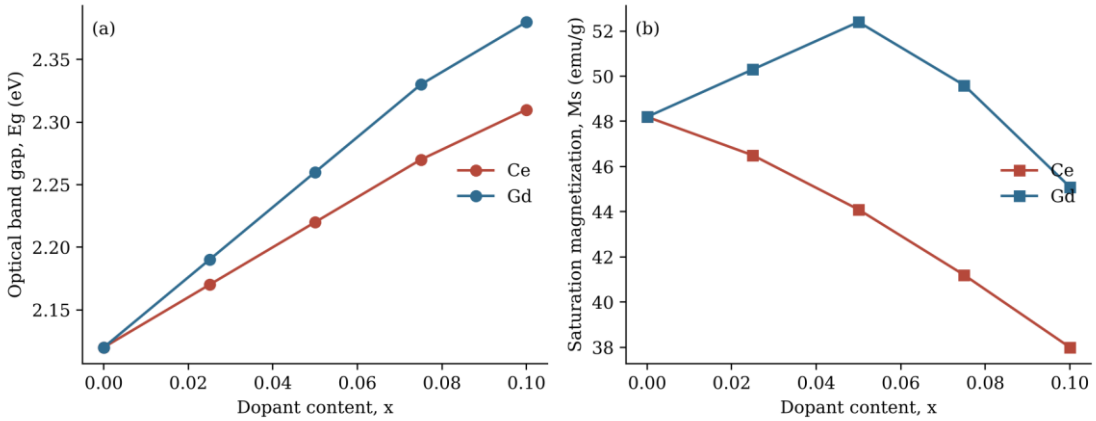


Figure 5. Dependence of (a) optical band gap and (b) saturation magnetization on Ce and Gd content.

Table 4- *Comparison of the present trends with related rare-earth-substituted nickel ferrites*

Study	Material and route	Optical behaviour	Magnetic behaviour
Yao et al. (2021)	$NiFe_{2-x}Gd_xO_4$ thin films (sol–gel); x = 0–0.1	Band gap increased with Gd content	M_s and M_r highest at x = 0.05, then sharp decline
Slimani et al. (2020)	$NiFe_{2-x}Dy_xO_4$ nanoparticles (sol–gel auto-combustion); x ≤ 0.10	Not reported in the cited abstract	Slight decrease in magnetization versus pristine ferrite; soft ferrimagnetic at 300 K and 10 K
Chandra et al. (2024)	$NiFe_{2-x}Gd_xO_4$ nanoparticles (citrate route)	Gd content tunes E_g, refractive index and related optical parameters	Not addressed

Study	Material and route	Optical behaviour	Magnetic behaviour
Agboola et al. (2022)	Nd-substituted $NiFe_2O_4$ (co-precipitation)	Not addressed	VSM parameters indicate suitability for switching and high-frequency devices
This work (Ce)	$NiFe_{2-x}Ce_xO_4$; x = 0–0.10	E_g: 2.12 → 2.31 eV	M_s: 48.2 → 38.0 emu/g (monotonic decrease)
This work (Gd)	$NiFe_{2-x}Gd_xO_4$; x = 0–0.10	E_g: 2.12 → 2.38 eV	M_s maximum 52.4 emu/g at x = 0.05

Note. Literature entries give a summary of the findings reported by the cited authors, and values are not directly comparable due to differences in synthesis route, the form of the material (film versus powder), and normalization.

3.6 Implications for applications

Results indicate practical guidelines. The substitution of Gd (around x = 0.05) would seem to be the most promising approach because it increases Ms and decreases Hc at the same time while maintaining the spinel content above 98% for high-frequency inductors and microwave components, where low coercivity and moderate-to-high magnetization are desired. Combined with the lower Urbach energy penalty at low x, the small widening of the gap observed in the Ce series allows for small x additions ($x \leq 0.05$) of either dopant without serious detriment, but larger Ce contents for the magnetic recoverable photocatalysts detract from both the magnetic recoverability and visible-light absorption. The higher the Ce content, the smaller the particle size and the lower the coercivity (rhenence) and the superior the crystallite size is, but the lower the saturation magnetization is, for superparamagnetic or biomedical applications, where low remanence and small particle size are desired.

There are a number of caveats that should be noted. Only room-temperature magnetizations have been measured so far, and the blocking behaviour and temperature dependence of the 4f–3d coupling are still not investigated. The distribution of cations was not actually measured, but derived from trends in structure and spectra; it would be determined by neutron diffraction or Mössbauer spectroscopy. No measurements of the valence of cerium were performed, and the Ce^{3+}/Ce^{4+} ratio could be determined by X-ray photoelectron spectroscopy (XPS). Finally, the range of dopants was limited to $x \leq 0.100$, and the smaller steps around x = 0.05 around the maximum of the magnetization would give a more precise definition of the maximum.

4. Conclusion

With this purpose, Ce and Gd-substituted nickel ferrite NiFe2−xRxO4 (x = 0.000–0.100) was synthesized using the sol–gel auto-combustion method, and structural, optical, and magnetic properties of the synthesized ferrite were compared. Both dopants enter the cubic inverse-spinel lattice at low concentration, expanding the lattice and refining the crystallites, but they exceed their solubility limits at about x = 0.025–0.050 and segregate as CeO_2 and $GdFeO_3$, respectively. The secondary-phase fraction remains below 3.5%.

The direct optical band gap widens from 2.12 eV to 2.31 eV with Ce and to 2.38 eV with Gd, an effect attributed to reduced Fe 3d–O 2p hybridization, lattice expansion, and carrier-density changes, and it is accompanied by an increase in Urbach energy and a decrease in refractive index. Ce substitution decreases the saturation magnetization monotonously from 48.2 to 38.0 emu/g, while Gd substitution increases it to the maximum value of 52.4 emu/g at x = 0.050, followed by a decrease till it becomes 45.1 emu/g. The coercivity is lower in both series, making them magnetically softer materials.

The overall conclusion from the above results is that the optical and magnetic properties of the $NiFe_2O_4$ could be tuned independently to a certain extent by altering the type and amount of rare earth elements and that the use of Gd with x~0.05 yields the best overall combination of wide band gap, high magnetization and low coercivity. Future work should focus on low-temperature magnetometry, direct determination of the optimum compositions, and the valence of cerium.

REFERENCES:

1. Agboola, P. O., Haider, S., & Shakir, I. (2022). The impact of rare earth Nd^{3+} cations on structural, spectral, magnetic and dielectric parameters of $NiFe_2O_4$ nanoparticles. *Journal of Taibah University for Science, 16*(1), 392–400. https://doi.org/10.1080/16583655.2022.2059953
2. Chandra, P., Shilpa, C. C., & Kumar, G. K. (2024). A study on fine-tuning the optical energy band gap and various optical parameters with the impact of gadolinium composition in NGFO ferrite nanoparticles. *Ukrainian Journal of Physics, 69*(5), 304.
3. Cullity, B. D., & Graham, C. D. (2009). *Introduction to magnetic materials* (2nd ed.). John Wiley & Sons.
4. Davis, E. A., & Mott, N. F. (1970). Conduction in non-crystalline systems V. Conductivity, optical absorption and photoconductivity in amorphous semiconductors. *Philosophical Magazine, 22*(179), 903–922.
5. Hervé, P., & Vandamme, L. K. J. (1994). General relation between refractive index and energy gap in semiconductors. *Infrared Physics & Technology, 35*(4), 609–615.
6. Kefeni, K. K., Msagati, T. A. M., & Mamba, B. B. (2017). Ferrite nanoparticles: Synthesis, characterisation and applications in electronic device. *Materials Science and Engineering: B, 215*, 37–55.
7. Moustafa, A. M., Ward, A. A., Mabied, A. F., & Gad, S. A. (2026). Impact of nickel doping on the optical, magnetic and electrical properties of CMFC ferrite. *Scientific Reports*. https://doi.org/10.1038/s41598-026-67441-w
8. Néel, L. (1948). Propriétés magnétiques des ferrites; ferrimagnétisme et antiferromagnétisme. *Annales de Physique, 3*, 137–198.
9. Patterson, A. L. (1939). The Scherrer formula for X-ray particle size determination. *Physical Review, 56*(10), 978–982.
10. Sankaranarayanan, R., Shailajha, S., Kairon Mubina, M. S., & Anilkumar, C. P. (2020). Effect of Ni^{2+} and Fe^{3+} ion concentrations on structural, optical, magnetic, and impedance response of $NiFe_2O_4$ nanoparticles prepared by sol-gel process. *Journal of Superconductivity and Novel Magnetism, 33*. https://doi.org/10.1007/s10948-020-05617-9
11. Shannon, R. D. (1976). Revised effective ionic radii and systematic studies of interatomic distances in halides and chalcogenides. *Acta Crystallographica Section A, 32*(5), 751–767.

12. Slimani, Y., Almessiere, M. A., Güner, S., Kurtan, U., Shirsath, S. E., Baykal, A., & Ercan, I. (2020). Magnetic and microstructural features of Dy3+-substituted $NiFe_2O_4$ nanoparticles derived by sol–gel approach. *Journal of Sol-Gel Science and Technology, 95*(1), 202–210. https://doi.org/10.1007/s10971-020-05292-1
13. Smit, J., & Wijn, H. P. J. (1959). *Ferrites: Physical properties of ferrimagnetic oxides in relation to their technical applications*. Philips Technical Library.
14. Tauc, J., Grigorovici, R., & Vancu, A. (1966). Optical properties and electronic structure of amorphous germanium. *Physica Status Solidi (b), 15*(2), 627–637.
15. Urbach, F. (1953). The long-wavelength edge of photographic sensitivity and of the electronic absorption of solids. *Physical Review, 92*(5), 1324.
16. Williamson, G. K., & Hall, W. H. (1953). X-ray line broadening from filed aluminium and wolfram. *Acta Metallurgica, 1*(1), 22–31.
17. Yao, H., Ning, X., Zhao, H., Hao, A., & Ismail, M. (2021). Effect of Gd-doping on structural, optical, and magnetic properties of $NiFe_2O_4$ as-prepared thin films via facile sol–gel approach. *ACS Omega, 6*(9), 6305–6311. https://doi.org/10.1021/acsomega.0c06097